Resource Characterization of Sites in the Vicinity of an Island near a Landmass

Resource Characterization of Sites in the Vicinity of an Island near a Landmass

Accepted Manuscript

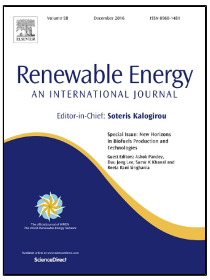

Resource Characterization of Sites in the Vicinity of an Island near a Landmass

Alberto Pérez-Ortiz, Alistair G.L. Borthwick, James McNaughton, Helen C.M. Smith, Qing Xiao

PII:	S0960-1481(16)30974-0
DOI:	10.1016/j.renene.2016.10.086
Reference:	RENE 8285
To appear in:	*Renewable Energy*
Received Date:	01 April 2016
Revised Date:	21 October 2016
Accepted Date:	26 October 2016

Please cite this article as: Alberto Pérez-Ortiz, Alistair G.L. Borthwick, James McNaughton, Helen C.M. Smith, Qing Xiao, Resource Characterization of Sites in the Vicinity of an Island near a Landmass, *Renewable Energy* (2016), doi: 10.1016/j.renene.2016.10.086

- Resource characterization of coastal sites defined as an island near a landmass
- Undisturbed kinetic or dissipated power do not approximate maximum power extracted
- Numerical results exceed those from an analytical model except for long islands
- Increased offshore depth and lower blockage both reduce the maximum power extracted
- Power extracted can be maximized with extraction in strait and offshore of island

Resource Characterization of Sites in the Vicinity of an Island near a Landmass

Alberto Pérez-Ortiz[1a], Alistair G. L. Borthwick[2], James McNaughton[3], Helen C. M. Smith[4] and Qing Xiao[5]

1 Industrial Doctoral Centre for Offshore Renewable Energy. Graduate School of Engineering, The University of Edinburgh, The King's Buildings, Faraday Building, Edinburgh, EH9 3JL, UK.
2 Institute of Energy Systems. The University of Edinburgh, The King's Buildings, Edinburgh, EH9 3JL, UK.
3 General Electric Renewable Energy. 214 Castlemead, Lower Castle Street, Bristol, BS1 3AG, UK.
4 College of Engineering, Mathematics and Physical Sciences, University of Exeter, Penryn Campus, TR10 9FE, Penryn, UK.
5 Department of Naval Architecture, Ocean and Marine Engineering, University of Strathclyde, G4 0LZ, Glasgow, UK.

Abstract

Renewable energy technologies are undergoing rapid development, the global aim being to achieve energy security and lower carbon emissions. Of marine renewable energy sources, tidal power has inherent predictability and large theoretical potential, estimated to exceed 8,000 $(TW.h)a^{-1}$ in coastal basins. Coastal sites in the vicinity of an island near a landmass are prime candidates for tidal stream power exploitation by arrays of turbines. This paper characterizes numerically the upper limit to power extraction of turbines installed at such sites. It is demonstrated that the maximum power extracted from the strait is generally not well approximated by either the power dissipated naturally at the seabed or the undisturbed kinetic power of flow in the strait. An analytical channel model [C. Garrett and P. Cummins, "The power potential of tidal currents in channels," Proc. R. Soc. A Math. Phys. Eng. Sci., vol. 461, no. 2060, pp. 2563–2572, Aug. 2005] provides lower predictions than the present numerical model of available power in the strait due to the analytical model not accounting for changes to the driving head resulting from power extraction and flow diversion offshore of the island. For geometrically long islands extending parallel to the landmass, the numerically predicted extracted power is satisfactorily approximated by the power naturally dissipated at the seabed, and there is reasonable agreement with the estimate by the channel analytical model. It is found that the results are sensitive to choice of boundary conditions used for the coastlines, the eddy viscosity, and bed friction. Increased offshore depth and lower blockage both reduce the maximum power extracted from the strait. The results indicate that power extracted from the site can be maximum if extraction is implemented both in the strait and offshore of the island. Presence of the landmass and increasing island dimensions both enhance power extraction.

Keywords

Tidal Energy; Resource Assessment; Numerical Modelling; Strait; Island; Landmass

[a] Corresponding author.
Present address: Suspro, 1 Diamond Street, Bristol, BS3 3LF, UK.
E-mail address: alberto.perez@suspro.net

1 Introduction

Development of renewable energy technologies has undergone remarkable progress in the past decades motivated by the security of supply, finiteness and unstable price of fossil fuels [1] [2] and the effects on the climate associated with carbon emissions [3]. Renewable energy sources such as wind and solar are stochastic and as such, backup generation is required during those time periods when generation is unable to meet demand. Tidal currents have the advantage of being completely deterministic, and therefore quite predictable, making power-grid integration more straightforward. The ebb and flow motions of tidal currents make tidal power production intermittent, and so backup would be required during slack water as the tide turns and possibly during neap tides. Tidal farms exploit the relatively high energy densities of tidal streams, thus limiting their footprint in comparison to wind and solar farms.

The first pre-commercial tidal arrays are under construction and in the next ten to twenty years it is expected that the first multi-megawatt commercial arrays will become operational. The success of such tidal projects depends on correct estimation of the tidal resource and assessment of the associated environmental impacts. Tidal energy comprises both potential and kinetic energy; hence resource assessment requires information on sea surface elevations and current velocities. Typically, data are measured at the site using acoustic Doppler current profilers (ADCP), and the tidal signal time history reproduced using harmonic analysis [4]. The data are very useful for validation of tide models. However, there are limits to ADCP deployment, owing to the cost of field measurement campaigns. Lack of spatial data coverage and measurement errors add to uncertainty in theoretical model calibration.

Power extraction alters the local flow hydrodynamics, and this must be accounted for in predictive models used for tidal resource assessment. Such models can be classified into three categories. Analytical one-dimensional (1D) models determine the maximum average power extracted from an idealised channel connecting two infinite ocean basins [5] or an infinite ocean basin with an enclosed bay [6] based on accessible parameters such as amplitude of tidal head difference driving the flow, peak flow through the channel, seabed friction, and channel dimensions. However, such analytical models assume idealised seabed conditions and channel geometry, and uniform power extraction. These limitations are largely overcome by using two-dimensional (2D) and three-dimensional (3D) models. 2D models solve the shallow water equations (SWE) to compute free surface elevations and depth-averaged velocities, and permit a localised representation of power extraction by tidal turbines. Although 2D models are computationally efficient, they neglect vertical flow behaviour. 3D models compute the flow velocity over the entire water column and model the power extraction profile over the water column, leading to a more realistic representation of power extraction. The resulting improvement in accuracy is at the expense of greatly increased computational load, limiting 3D models to small- and medium-scale domains, unlike 2D models which are routinely applied to medium- to large-scale domains [7].

Draper [8] identified four generic coastal sites suitable for tidal energy exploitation: strait between two infinite ocean basins; enclosed bay; headland; and strait between an island and a semi-infinite landmass. The case of a channel linking two infinite ocean basins has been analysed analytically by Bryden and Couch [9], Vennell [10] and Garrett and Cummins [5] (GC2005). The GC2005 channel model computes the maximum average power available for extraction, also called the potential of the channel, based on the head driving the flow, the maximum volumetric flow rate through the channel and the phase difference between the driving head and flow in the channel. The model assumes that the flow is driven by a constant head, independent of the level of power extraction, and that the flow cannot divert from the

channel. The model predicts that the maximum average power available is greater, for a short channel carrying a strong current, and lower, for a long channel carrying a slower current, than the average undisturbed kinetic power through the most constricted cross-section of the channel. In addition, the model predicts that at maximum power extracted, the flow through the channel is reduced to 57.7% of the flow in undisturbed conditions. Draper *et al*. [11] assessed the limits to power extraction in the Pentland Firth, a strait located between the north coast of Scotland and the geometrically long and wide Orkney Islands, and found the results to agree with the power extraction predictions by GC2005. Agreement between numerical results and GC2005 model was also found by Sutherland *et al*. [12] for the Johnstone Strait, located between the geometrically long Vancouver Island and the west coast of Canada. The potential of a channel linking an infinite ocean basin to an enclosed bay has been analysed analytically by Garrett and Cummins [13] and Blanchfield *et al*. [6]. Numerical results by Draper [8] compared favourably to predictions by Blanchfield *et al*. [6] for an isolated bay. Draper *et al.* [14] analysed the potential of an array deployed near an idealised headland and the effects of power extraction by the array on the environment. The potential of the array was generally not well approximated by either the local undisturbed power or the power naturally dissipated by the seabed. Serhadlıoğlu *et al*. [15] obtained similar findings in their assessment of power extraction off the Anglesey Skerries, north-west of Wales. The coastal site defined as a strait between an island and a semi-infinite landmass may be sub-classified as follows: island of similar length and width in the vicinity of a landmass; isolated offshore island; island that is geometrically long and/or wide in the vicinity of a landmass; and isolated offshore multi-island system. Draper [8] numerically investigated the potential of a strait between a long and wide island and a landmass, and found that the maximum averaged power extracted was not well approximated by the GC2005 channel model. The disparity in the results arose from changes in the driving head induced by power extraction, with minimal bypass flow offshore of the island. Limits to power extraction in multiple-channel coastal sites can also be assessed through an electrical circuit analogy, whereby the head driving the flow is represented by an alternating voltage, the flow is represented by the electric current, and bed friction and turbines correspond to non-linear resistances [8]. The electrical analogy theory has been employed by Draper *et al*. [16] to assess the resource of the Pentland Firth, located between north coast of Scotland and the Orkney Islands, and by Cummins [17] to investigate the power potential of a split tidal channel.

Coastal sites categorized as a channel linking two infinite ocean basins could also be categorized as a strait between an island and landmass. This paper analyses numerically the limits to power extraction at idealised sites in the vicinity of an island near a landmass by means of a sensitivity analysis, and explores under which conditions the flow dynamics in the strait behave similarly to that in a channel linking two infinite ocean basins. This paper is structured in four sections. Section 2 details the methodology employed in the analysis of the coastal site. Section 3 presents the analysis and discussion of the island-landmass coastal site. Section 4 summarises the conclusions.

2 Methodology

This section describes the methodology employed to undertake a resource assessment of power extraction from a strait between an island and landmass. First, the numerical model employed for the analysis is described. Second, the parameterization of the numerical model is outlined. Third, the process of mesh convergence and spatial discretization of the domain is presented. The resource assessment methodology presented herein has previously been verified and validated by Pérez-Ortiz *et al*. [18] [19].

2.1 Numerical Model

This study is carried out using the finite element numerical code Fluidity [20] which solves the non-conservative form of the shallow water equations:

$$\frac{\partial \eta}{\partial t} + \nabla \cdot (h\overline{u}) = 0 \quad (1)$$

$$\frac{\partial \overline{u}}{\partial t} + \overline{u} \cdot \nabla \overline{u} + g\nabla\eta + C_d \frac{|\overline{u}|\overline{u}}{h} = 0 \quad (2)$$

where η is the elevation of the free surface above mean water level, $\overline{u}$ is the horizontal velocity vector, t is time, ∇ is the horizontal gradient vector, h is the total water depth, g is the acceleration due to gravity, and C_d is the bottom drag coefficient. The model setup follows guidelines for coastal and tidal power extraction modelling provided by the Fluidity developers [21] [22]. Based on results from Cotter *et al*. [20] for large-scale ocean applications solving the SWE, a mixed finite element discretization scheme $P_{1DG}P_2$ is employed, which is linear discontinuous Galerkin for velocity and quadratic continuous Galerkin for pressure. The backward Euler scheme is employed to temporally discretise the momentum equation [23]. Velocity and pressure fields are resolved using a Generalised Minimal Residual Method (GMRES) solver with a Successive Over-Relaxation (SOR) pre-conditioner [21]. The tolerance in the absolute error solution and maximum number of iterations are specified as 10^{-7} and 1,000 respectively for both pressure and velocity fields.

2.2 Model Parameterization

Figure 1 depicts the coastal model parameters. The model domain is defined by five boundaries: open boundaries Γ_1 and Γ_4 at the east and west limits of the domain; a solid boundary Γ_2 in the north; a solid boundary Γ_3 in the south corresponding to the semi-infinite landmass; and a solid boundary Γ_5, corresponding to the island. Boundaries Γ_3 and Γ_5 define the strait.

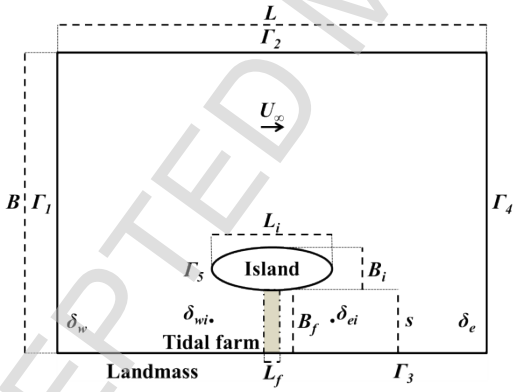

Figure 1. Model geometry and tidal parameters for a strait between an island and a semi-infinite landmass. Grey area indicates the tidal array.

The geometry of the domain is defined by its length L, width B and water depth h_o. The width B is set so that the free stream velocity U_∞ is fully developed north of the island. The island geometry is ellipsoidal with length L_i and width B_i. The parameter s, corresponding to the minimum distance between island and landmass, defines the width of the strait. Sea surface elevations above mean sea level at the west and east open boundaries are defined as δ_w and δ_e respectively. Unless otherwise stated, model seabed friction is characterized by a dimensionless drag coefficient C_d = 0.0025. Turbulence is included using an empirical depth-averaged parabolic eddy viscosity ν_t [24].

$$\nu_t = \frac{k}{6}\left[C_d\left(u^2 + v^2\right)\right]^{1/2} h \quad (3)$$

where k = 0.41 is the von Kármán constant, u and v are the stream-wise and transverse velocity components.

Unless otherwise stated, the water depth h_o in the domain is fixed at 40 m in the stream-wise direction between (transverse) cross-sections located $0.36L$ upstream and downstream of the centre of the island. From cross-sections located $0.36L$ to $0.43L$ upstream and downstream of the island's centre, the water depth is linearly increased from h to $75h$ in the stream-wise direction, and kept to $75h$ in the remaining part of the domain. The increase in water depth near the open boundaries mimics conditions at the edge of the continental shelf. The deep water zone attenuates reflected long waves from the island and power extraction zone and reflects them back onto the shelf before such waves reach the open boundaries [25].

Three scenarios are considered in order to define conditions at the solid boundaries of the island and landmass: a free-slip condition; a no-slip condition; and a non-uniform seabed scenario where the water depth is increased linearly from $0.125h_o$ at the island and landmass boundaries to h_o at a distance $0.1\emptyset_i$ away from both solid boundaries, and a free-slip condition is applied to island and landmass. Here, $\emptyset_i$ is the diameter of the island in the case where the length of the island L_i is the same as its width B_i. In all scenarios, a free-slip boundary condition is set at north solid boundary Γ_2. Open boundary conditions are prescribed as follows: zero surface elevation at Γ_4; and free surface elevation at Γ_1 computed for the M_2 tidal constituent from:

$$\delta_w = a_o a\sin\left(\omega_t t\right) \quad (4)$$

where a and ω_t are the amplitude and frequency of the M_2 tidal wave (3 m and 1.41 x 10^{-4} rad/s respectively). The parameter a_o is used to minimize the formation of perturbations by ramping up the tidal signal over the first two tidal cycles:

$$a_o = 0.5\left(1 - \cos\left(\frac{\omega_t t}{4}\right)\right) \quad (5)$$

Other site-dependent parameters such as Coriolis force, atmospheric pressure, wind or wave conditions are not included in the numerical model. The time step is chosen accordingly, to limit the Courant-Friedrichs-Lewy number to be within O(1).

The area of power extraction, or tidal farm, is located at the central and narrowest section of the strait, and it is defined by a length L_f and a width B_f. The presence of turbines is included in the model through the addition of an equivalent seabed friction coefficient k_f in the farm area A_f, which is treated implicitly in the same way as natural seabed friction [12] [26]. This methodology of power extraction does not account for turbine-scale losses, for example due to mixing behind fences or arrays of tidal turbines; consequently the results represent an upper limit to power extraction [27].

2.3 Spatial discretization of the Model

The domain is spatially discretized based on the results of a mesh convergence analysis for the case of a circular island ($L_i = B_i = \emptyset_i = 50h_o$) and strait width $s = L_i$ for free-slip and no-slip scenarios under steady-state conditions with the flow travelling from west to east of the domain. The mesh is defined by specifying the element edge length on four different boundary regions: on the landmass and within $2\emptyset_i$ of the island, the rest of the landmass, on the island, and the north boundary. Six meshes are generated using Gmsh [28] with Table I listing the mesh-

edge length definition and the total number of mesh elements. Convergence of the velocity solution is analysed at four transverse cross-sections of length $5Ø_i$ extending from the landmass located $Ø_i$ west of the island centre, at the island centre, and $Ø_i$ and $2Ø_i$ east of the island centre.

Table I. Six spatial discretization cases considered in mesh convergence analysis. Element edge length used in the three mesh regions of the model, and total number of mesh elements.

	Element edge length				
Mesh	Landmass		Island	North boundary	Mesh elements
	$> 2Ø_i$	$\leq 2Ø_i$			
1	$\pi Ø_i /6$	$\pi Ø_i /6$	$\pi Ø_i /12$	$\pi Ø_i$	3,902
2	$\pi Ø_i /6$	$\pi Ø_i /6$	$\pi Ø_i /28$	$\pi Ø_i$	6,156
3	$\pi Ø_i /17$	$\pi Ø_i /28$	$\pi Ø_i /36$	$\pi Ø_i$	9,968
4	$\pi Ø_i /17$	$\pi Ø_i /36$	$\pi Ø_i /76$	$\pi Ø_i$	13,658
5	$\pi Ø_i /17$	$\pi Ø_i /76$	$\pi Ø_i /156$	$\pi Ø_i$	27,498
6	$\pi Ø_i /17$	$\pi Ø_i /156$	$\pi Ø_i /316$	$\pi Ø_i$	62,526

For the free-slip scenario, mesh independence is achieved at the four cross-sections for Mesh 4. For the no-slip scenario, analysis of the stream-wise velocity component at the island centre cross-section shown in Figure 2*a* appear to indicate that mesh convergence is satisfied at the island using Mesh 4. However, results at cross-section $2Ø_i$ east (downstream) of the island (Figure 2*b*) indicate that full convergence of the velocity field has not been achieved. Although the wake behind the island is not accurately reproduced in the no-slip scenario, results from a validation test of flow past a surface piercing circular cylinder by Pérez-Ortiz *et al*. [18] have shown that Mesh 4 is able to capture the main flow features around the island. In the next section several scenarios are considered to assess the influence of the parameters defining the geometry (see Figure 1). Meshes for each of these scenarios are created based on the Mesh 4 edge-length specifications in Table I; Figure 3 presents these domains.

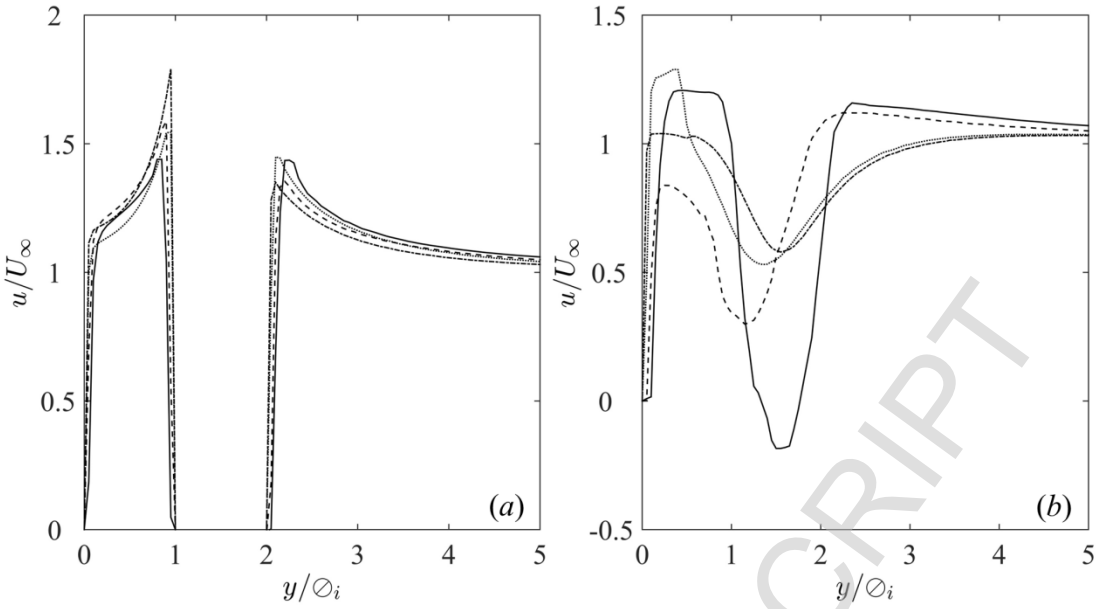

Figure 2. Stream-wise flow velocity profile at transverse cross sections at (*a*) the island centre cross-section, and (*b*) $2\emptyset_i$ east of the island centre. The model is run with no-slip boundary conditions at island and coastline. Fluidity predictions for Mesh 3 (solid line), Mesh 4 (dashed line), Mesh 5 (dotted line) and Mesh 6 (dash-dot line).

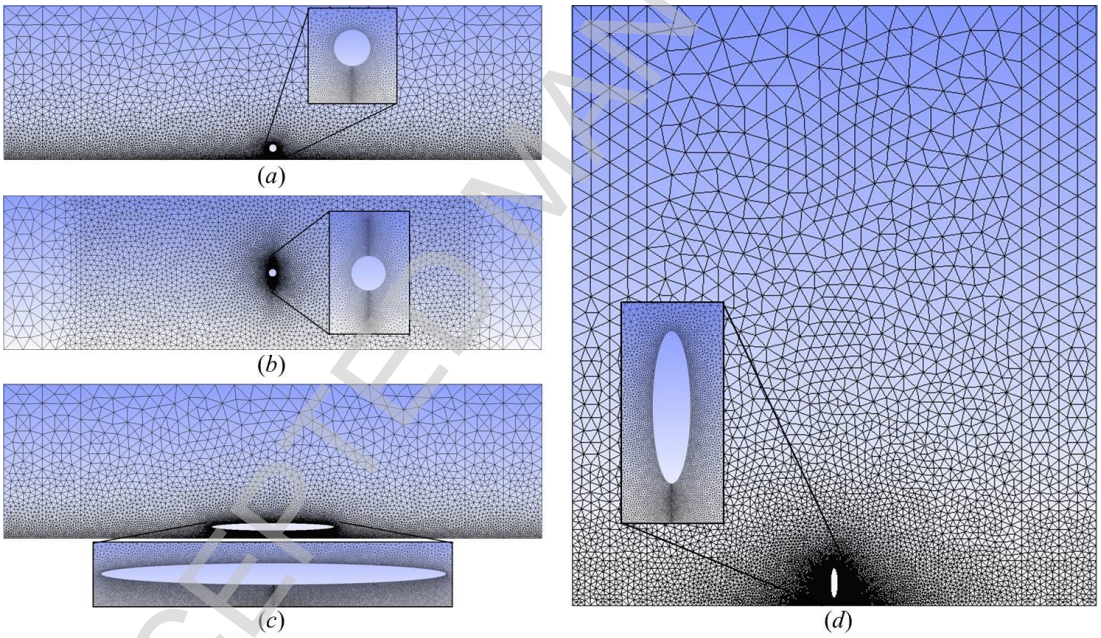

Figure 3. Unstructured spatial discretization: (*a*) Island in the proximity of a semi-infinite landmass; (*b*) isolated offshore island; (*c*) geometrically long island; and (*d*) geometrically wide island. A regular biased-right isosceles triangles grid is used to delineate the tidal farm

3 Analysis

This section presents and discusses results from a sensitivity analysis of the tidal power resource of sites in the vicinity of an island near a landmass, hereby referred to as the island-landmass system. For each case presented, simulations are run for seven tidal periods *T*: during

the first two tidal periods the system is ramped up; the following two tidal periods correspond to spin-up of the system; the final three tidal periods are used for resource assessment.

3.1 Island in Proximity of a Semi-infinite Landmass

First the tidal resource of an island-landmass system is assessed. Then a sensitivity analysis is carried out concerning the impact of changing the friction, eddy viscosity, offshore water depth, blockage ratio, and combined strait-offshore power extraction. The island has dimensions $L_i = B_i = \emptyset_i = 50h_o$, and is located a distance $s = \emptyset_i$ from the landmass. The domain has length $L = 70\emptyset_i$ and width $B = 20\emptyset_i$. The mesh contains 8,027 vertices and 16,054 elements, and a regular grid of 80 biased-right isosceles triangles defines the area where power extraction is implemented, located at the narrowest section of the strait (Figure 3*a*). Three scenarios are considered for the boundary conditions (as mentioned in Section 2.2). Figure 4 presents vorticity contour plots for the three scenarios, at times $T/2$ and T. Vortex shedding occurs in the lee of the island for a no-slip boundary condition set at the island, and for the non-uniform seabed scenario, but not for a free-slip boundary at the island.

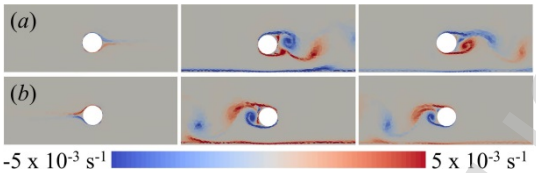

Figure 4. Vorticity contour plots for the free-slip (left), no-slip (centre) and non-uniform seabed (right) scenarios taken at: (*a*) $t = T/2$; and (*b*) $t = T$.

Figure 5 shows contour plots of the speed and kinetic power density, computed from the stream-wise and transverse velocity components, averaged over three tidal cycles, obtained for the free-slip scenario. Higher velocities and consequent kinetic power densities are predicted to occur in waters to the immediate south and north of the island.

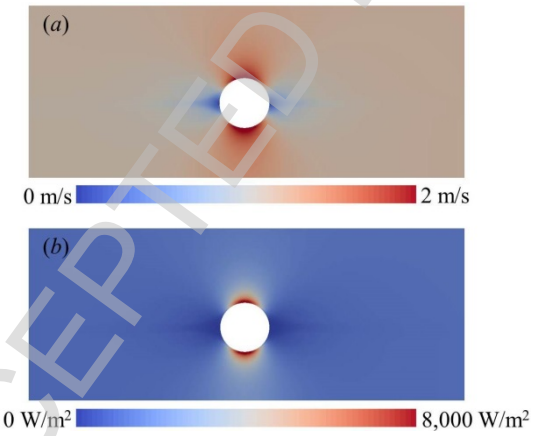

Figure 5. Contour plots of the three-tidal-cycle averaged speed (*a*) and kinetic power density (*b*) for the free-slip scenario, where flow travels from west to east and east to west at flood and ebb tide respectively.

For the three scenarios, power extraction levels k_f between 0 and 4.5 are implemented at the tidal farm in the strait. Figure 6 shows three tidal period-averaged results: undisturbed kinetic power $\overline{P}_{ko}$, defined as the kinetic power evaluated at the narrowest section of the strait with no power extraction and computed from the stream-wise and transverse velocity components; natural power dissipated at the seabed in the strait in the absence of power extraction $\overline{P}_s$;

kinetic power in the strait $\overline{P}_k$ with the tidal farm present; and power extracted from the flow by the tidal farm $\overline{P}_e$. There is a clear disparity in the predictions between the three scenarios evident in the kinetic and extracted power plots. The discrepancy in results between the free-slip and no-slip scenarios may be explained by flow separating at the island in the no-slip scenario. The no-slip and free-slip scenarios may represent upper and lower bounds to power extraction in the strait, with the value of power extracted for the non-uniform seabed scenario falling in-between the values for the no-slip and free-slip scenarios. No clear relationship is found between the maximum $\overline{P}_e$ in the strait and $\overline{P}_s$. For the no-slip scenario, the results indicate that maximum power extracted could be approximated by $\overline{P}_{ko}$; however this is not the case for the free-slip and non-uniform seabed scenarios. Rates of decrease of $\overline{P}_k$ are higher for the free-slip and non-uniform seabed scenarios than for the no-slip scenario at low extraction levels $k_f < 0.5$, but they are relatively similar when $k_f > 0.5$.

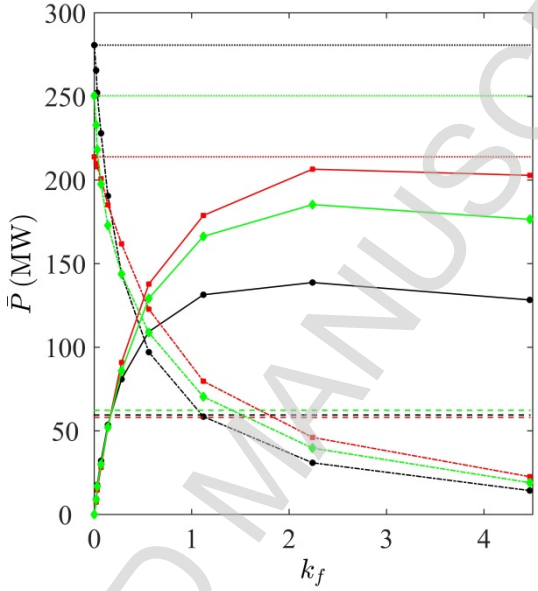

Figure 6. Power profiles as functions of k_f for a strait between an island and landmass: free-slip (black), no-slip (red) and non-uniform seabed (green) scenarios. Extracted power for a tidal farm located in the strait $\overline{P}_e$ (solid line); kinetic power for the strait with the tidal farm present $\overline{P}_k$ (dash-dot line); kinetic power for undisturbed conditions in the strait $\overline{P}_{ko}$ (dotted line); and natural power dissipated on the seabed at the strait $\overline{P}_s$ (dashed line). Markers indicate output data from the numerical model.

Unlike a channel connecting two infinite ocean basins, the island-landmass is a two-path flow system, where under equal water depths and bottom friction conditions, both paths exert relatively similar resistance to the flow, noting that the presence of the landmass increases the resistance of the strait path. The volumetric flow rate, $\overline{Q} = uh_o l$, is computed along two cross-sections of length $l = s$; one across the narrowest section of the strait, and the second spanning offshore from the northern limit of the island. Figure 7 plots the volumetric flow rates in the strait and offshore for the three scenarios. Values are normalised by the volumetric flow rate in the absence of power extraction $\overline{Q}_o$. Diminishing trends of volumetric flow rate across the strait are in agreement with the trends of kinetic power shown in Figure 6. In all three scenarios, the reductions in volumetric flow rates across the strait do not yield equivalent increases in volumetric flow rate offshore of the island, implying that there is some energy lost in the system

due to power extraction in the strait. The ratios $\overline{Q}/\overline{Q}_o$ at maximum $\overline{P}_e$ are equal to 1.21, 1.09 and 1.14 for the free-slip, no-slip and non-uniform seabed scenarios respectively.

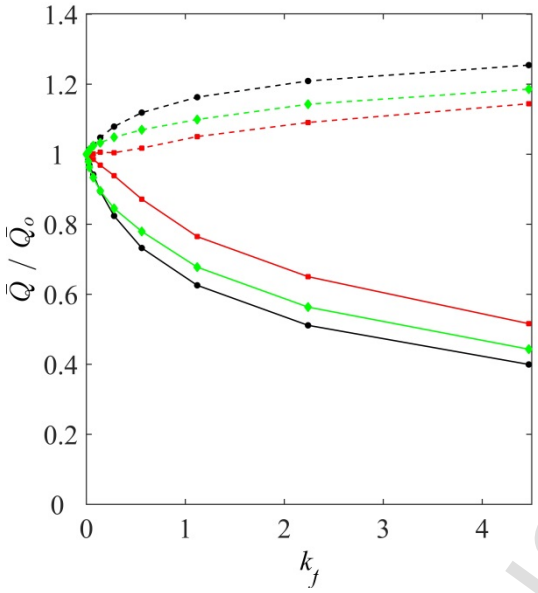

Figure 7. Changes in ratio of actual to undisturbed volumetric flow rate for free-slip (black), no-slip (red), and non-uniform seabed (green) scenarios at different levels of power extraction. Volumetric flow rates are calculated across the tidal farm (solid line) and through a cross-section of identical length at the offshore side of the island (dashed line). Markers indicate output data from the numerical model.

Analysis of Figure 6 and Figure 7 reveals that the volumetric flow rate through the strait at maximum power extracted is reduced to a range between 60-40 % of $\overline{Q}_o$ for the three scenarios, which approximates reasonably well to the 57.7 % volumetric flow rate predicted by GC2005 and Bryden and Couch [29].

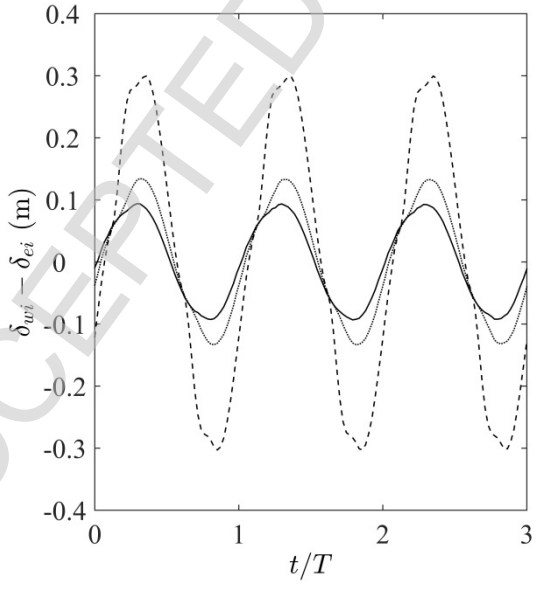

Figure 8. Flow driving head between entrance and exit of the strait for the free-slip scenario: no power extraction (solid line); low extraction k_f = 0.14 (dotted line); and very high extraction k_f = 2.24 (dashed line).

Figure 8 plots the head driving the flow in the strait $\delta_{wi} - \delta_{ei}$ (Figure 1) over three tidal periods for the free-slip scenario with varying values of k_f. The driving head increases as power extraction level in the strait rises from low (k_f = 0.14) to high (k_f = 2.24) power extraction levels. This agrees with numerical results from Draper [8] for a strait between an island with a high width to length ratio and a landmass.

In the free-slip scenario, based on the amplitude of the head driving the flow and maximum $\overline{Q}_o$ in the strait, the GC2005 channel model with γ = 0.22, where γ accounts for the phase difference between the driving head and flow in the channel, predicts a maximum extracted power in the order of about 45 MW. If γ is approximated by 0.2, as the peak flow lags the peak head drop along the strait by 35°, this leads to a predicted maximum power extracted of 40.7 MW. These values are 67.7 % and 78.3 % lower than the numerically computed free-slip values. For the no-slip scenario, the maximum power extracted is predicted to be 81.6 and 77.9 MW for γ = 0.22 and 0.21 (corresponding to peak flow lagging the peak head drop by 5º), which are 60.5 % and 62.3 % lower than the numerical estimates of maximum power extracted. It may be concluded that the GC2005 channel model is not applicable in this case, where the island geometry scale does not prevent bypass flow effects, and where the head driving the flow increases significantly with power extraction. The increase in driving head across the strait may also lead to higher bypass flow rates, distorting furthermore the comparison between the numerical predictions and GC2005.

3.1.1 Friction and Eddy Viscosity

Bottom friction is often used as a calibration parameter when modelling actual coastal sites [30]. Sensitivity of $\overline{P}_e$ in the strait to the choice of bottom friction is tested for three dimensionless coefficients C_d = 0.00125, 0.0025 and 0.005 [31]. Figure 9 plots the three-tide-period-averaged results of $\overline{P}_{ko}$, $\overline{P}_s$, $\overline{P}_k$ and $\overline{P}_e$ for the three assessed C_d values. Since the boundary conditions are kept constant, the lowest value of C_d consequently yields the highest $\overline{P}_{ko}$ kinetic power in the strait. More power is naturally dissipated by the seabed as C_d is increased. Higher $\overline{P}_e$ is achieved for lower C_d as less power is naturally dissipated by the bottom and there is more power available for extraction by the tidal farm in the strait. Figure 9 highlights the sensitivity of the tidal resource assessment to the parameterization of the domain friction environment, as analysed by Adcock *et al*. [30] for the Pentland Firth.

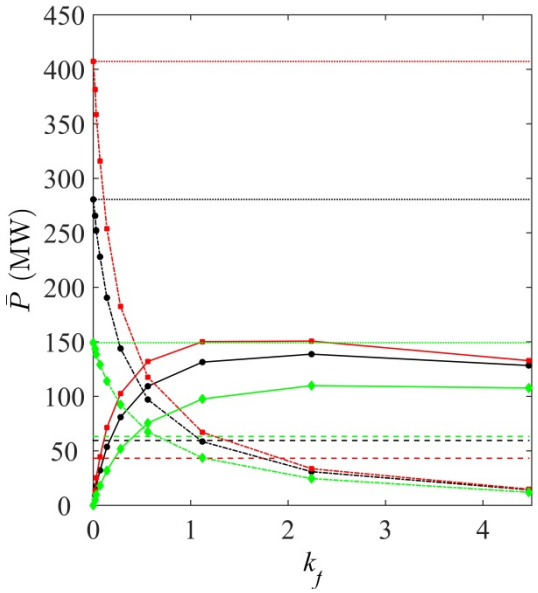

Figure 9. Power profiles as functions of k_f for a strait between an island and landmass: C_d = 0.0025 (black), C_d = 0.00125 (red) and C_d = 0.005 (green) scenarios. Extracted power for tidal farm located in the strait $\overline{P}_e$ (solid line); kinetic power for the strait with the tidal farm present $\overline{P}_k$ (dash-dot line); kinetic power for undisturbed conditions in the strait $\overline{P}_{ko}$ (dotted line); and natural power dissipated on the seabed at the strait $\overline{P}_s$ (dashed line).

The changes to the domain's frictional environment are also reflected in the bypass flows. At maximum $\overline{P}_e$, the offshore ratios $\overline{Q}/\overline{Q}_o$ are 1.25, 1.21, and 1.17 for C_d equal to 0.00125, 0.0025, and 0.005, respectively. Higher bypass flows are obtained with lower C_d.

Calibration of actual coastal site numerical models is also often performed using the eddy viscosity [32]. Sensitivity of $\overline{P}_e$ to the choice of eddy viscosity is assessed in the free-slip and no-slip scenarios using Eq. (3) with constant kinematic viscosity values of ν_t = 10^{-6}, 1, and 100 m^2s^{-1}, which correspond to the water molecular kinematic viscosity and two typical eddy viscosity values used in the calibration of numerical models [32]. For k_f levels equal to 0, 0.14 and 2.24, the resulting $\overline{P}_k$ and $\overline{P}_e$ are very similar, for both free-slip and no-slip scenarios, with the empirical depth-averaged parabolic (range of ν_t = 10^{-2} - 1 m^2s^{-1} in the vicinity of the island) and constant (ν_t = 10^{-6} and 1 m^2s^{-1}) values of depth-averaged eddy viscosity coefficient. The case with ν_t = 100 m^2s^{-1} yields different kinetic and extracted power results, and this difference is greater for the no-slip than free-slip scenario. At k_f = 2.24, comparison of results for constant ν_t = 100 m^2s^{-1} with those from the empirical formula for depth-averaged parabolic viscosity showing that $\overline{P}_k$ and $\overline{P}_e$ both increase by 19 % for free-slip and both reduce by 47 % for no-slip.

3.1.2 Water depth

In nature, the water depth offshore of an island is usually greater than in the strait of an island-landmass system. To analyse this effect on tidal resource estimates for the idealised strait, the water depth offshore of the island in the non-uniform seabed scenario is increased linearly northwards from $0.125h_o$ at the island to $4h_o$ at a distance $0.4Ø_i$ north of the island. Water depth is increased linearly from h_o to $4h_o$ west and east of the island along the landmass from the island centre plane until the continental shelf limits are encountered. Figure 10 compares the three-tide-period-averaged $\overline{P}_{ko}$, $\overline{P}_s$, $\overline{P}_k$ and $\overline{P}_e$ power profiles obtained when the water depth

offshore is set to h_o and $4h_o$. No changes are observed in $\overline{P}_{ko}$ and $\overline{P}_s$, implying that increase in water depth offshore does not alter the main undisturbed flow conditions in the strait. However, when the water depth is increased from h_o to $4h_o$ offshore, $\overline{P}_k$ decreases at a higher rate for the same k_f level and maximum $\overline{P}_e$ decreases from 180 MW to 130 MW. Increase in water depth offshore of the island reduces resistance to the flow in the offshore path, leading to higher bypass flow rates when extraction level in the strait is increased. This observed reduction in maximum $\overline{P}_e$ highlights the need for tidal site developers to have a detailed understanding of the effect of far-field bathymetry on power extraction by a tidal farm.

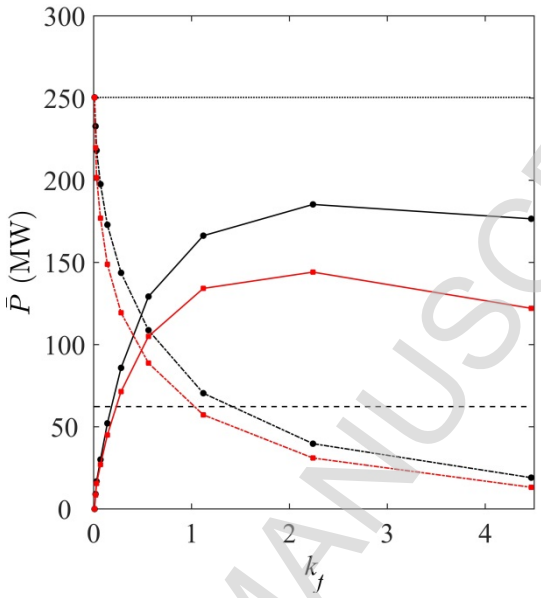

Figure 10. Power profiles as functions of k_f for a strait between an island and landmass: depth h_o offshore (black) and depth $4h_o$ offshore (red). Extracted power for tidal farm located in the strait $\overline{P}_e$ (solid line); kinetic power for the strait with the tidal farm present $\overline{P}_k$ (dash-dot line); kinetic power for undisturbed conditions in the strait $\overline{P}_{ko}$ (dotted line); and natural power dissipated on the seabed at the strait $\overline{P}_s$ (dashed line).

3.1.3 Farm Strait Blockage

Deployment of tidal turbines at coastal sites is constrained by technical, commercial, environmental and social factors. Resource estimates may be sub-optimal if the tidal farm cannot block the entire strait [33]. Based on the non-uniform seabed scenario of the island-landmass system, three cases are analysed: turbines installed across the entire cross-section of the strait, independent of water depth, hence the strait is 100 % blocked by the farm; turbines solely installed at depths equal or greater to h_o, representing an effective 80 % blockage of the strait; and turbine installation constrained by minimum water depth and environmental regulations setting minimum clearances between farm and island, and farm and landmass of $0.2\emptyset_i$ in both cases, leading to an effective strait blockage of 60 %. The reduction in strait blockage leads to two alternative bypass paths in the strait: between tidal farm and southern tip of island, and between tidal farm and landmass.

Figure 11 plots the three-tidal-period-averaged $\overline{P}_{ko}$, $\overline{P}_s$, $\overline{P}_k$ and $\overline{P}_e$ profiles for three strait-blockage ratio cases, as functions of the equivalent number of turbines in the farm N_T, derived from k_f as follows:

$$k_f = \frac{N_T(C_T A_T + C_D A_S)}{2A_f} \quad (6)$$

where A_T and A_S are respectively the projected area of the rotor and support structure (A_S = $0.1A_T$) of a 1 MW power-rated P_R tidal turbine with 20 m diameter rotor; C_T and C_D are the thrust and drag turbine coefficients (assumed constant and equal to 0.8 and 0.9 respectively).

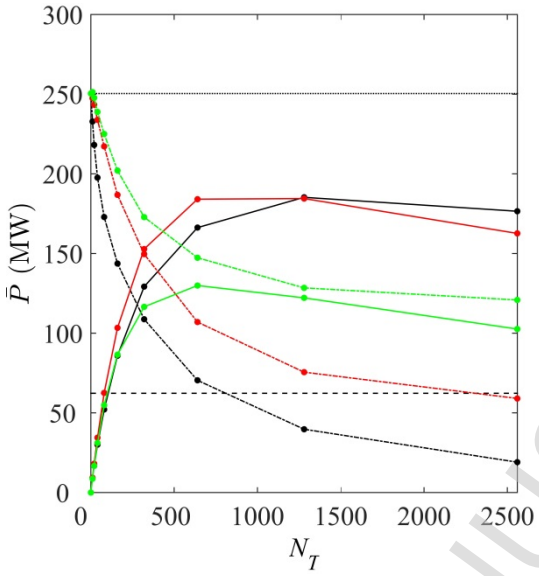

Figure 11. Power profiles as functions of N_T for a strait between an island and landmass for three extraction blockage ratios in the strait: 100 % (black); 80 % (red); and 60 % (green). Extracted power for tidal farm located in the strait $\overline{P}_e$ (solid line); kinetic power for the strait with the tidal farm present $\overline{P}_k$ (dash-dot line); kinetic power for undisturbed conditions in the strait $\overline{P}_{ko}$ (dotted line); and natural power dissipated at the seabed in the strait $\overline{P}_s$ (dashed line).

Similar values of maximum $\overline{P}_e$ are obtained for the 100 % and 80 % blockage ratio cases, and a lower maximum $\overline{P}_e$ is predicted for the 60 % case. The increase in frictional resistance due to reduction in water depth between farm and island and farm and landmass is found to limit bypass flow; this explains why the 80 % and 100 % blockage ratio cases yield similar estimates of maximum $\overline{P}_e$. From these results, it appears that implementation of power extraction in shallow regions of the strait using turbines of smaller size and power rating may not be necessary to reduce or prevent bypass flow. As the strait blockage ratio reduces, so do the rates of reduction of $\overline{P}_k$ in the strait with power extraction, as the flow reduction through the farm is counterbalanced by an increase of flow in the strait bypass regions. At high levels of power extraction and partial strait blockage, the increase of velocity in the bypass regions could lead to local seabed erosion in the long term.

3.1.4 Offshore Power Extraction

Although the water depth is likely to be deeper on the offshore side of an island, such a flow regime may still be suitable for tidal power generation (e.g. the Outer Sound, Pentland Firth, Scotland [30]). With development of deep water tidal technology, it is therefore worth exploring the limits to power extraction offshore of the idealised island as well as those for the two-path island-landmass system. Based on the free-slip scenario, power extraction is included on the offshore side of the island over a rectangular area of equal dimensions (L_f x B_f) to the tidal farm in the strait used in the island-landmass system. The farm extends towards the north of the

domain from the northern limit of the island, and is located at the same stream-wise coordinates as the farm in the strait. The addition of the offshore farm increases blockage of the domain by 50 %; however, no effect on the resource assessment is expected because of the large width of the domain. The averaged power generated by the farm $\overline{P}_T$ is computed from the local velocities and the following C_P function (based on the turbine described in Section 3.1.3):

$$C_P = \begin{cases} 0 & \text{if} \quad U < U_C \\ 0.4 & \text{if} \quad U_C \le U \le U_R \\ \dfrac{2P_R}{\rho A_T U^3} & \text{if} \quad U > U_R \end{cases} \qquad 7)$$

with cut-in speed U_C of 1m/s and rated speed U_R of 2.5 m/s.

Based on $\overline{P}_T$, N_T and P_R, the capacity factor *CF* of the tidal farm during the three tidal cycles is computed from:

$$CF = \frac{\overline{P}_T}{N_T P_R} \qquad 8)$$

Table II lists the three-tide-period-averaged parameters, $\overline{P}_T$, farm *CF*, velocity deficit $\overline{U}_o^*$ and kinetic power deficit $\overline{P}_k^*$, for six power extraction scenarios at the strait and offshore side of the island. Values of $\overline{P}_T$ and *CF* obtained in the strait or offshore side of the island are similar for the same k_f value. When k_f = 0.14 is applied both in the strait and offshore of the island (Scenario 5), there is a 50 % increase in $\overline{P}_T$ compared to Scenarios 1 and 3 where k_f = 0.28 is applied solely at one side of the island, in agreement with the lower $\overline{U}_o^*$ and $\overline{P}_k^*$ also evident for Scenario 5. Similar results are observed when comparing results from Scenario 6 with k_f = 0.28 applied to both sides of the island, against those from Scenarios 2 and 4. The data listed in Table II indicate that power generation in an island-landmass system may be optimized if considered as a two flow path problem, although complex bathymetry and flow conditions may require numerical optimization.

Table II. Extraction levels k_f and equivalent number N_T of turbines in the strait (S) and offshore side (O) of the island. The table lists values for the (three-tide) period-averaged array power generated $\overline{P}_T$, tidal farm capacity factor *CF*, percentage decrease in mean strait velocity $\overline{U}_o^*$, and percentage decrease in mean kinetic power $\overline{P}_k^*$.

Scenario	1		2		3		4		5		6	
Island Side	S	O	S	O	S	O	S	O	S	O	S	O
k_f	0.28	0	0.56	0	0	0.28	0	0.56	0.14	0.14	0.28	0.28
N_T	160	0	320	0	0	160	0	320	80	80	160	160
$\overline{P}_T$ [MW]	35.5	n.a.	47.2	n.a.	n.a.	35.3	n.a.	48.5	27.9	25.8	50.0	46.9
CF [%]	22.2	n.a.	14.8	n.a.	n.a.	22.0	n.a.	15.1	34.8	32.3	31.3	29.3
$\overline{U}_o^*$ [%]	-17.7	+3.6	-26.9	+7.5	+12.3	-14.4	+17.4	-23.2	-4.5	-3.2	-8.4	-6.2
$\overline{P}_k^*$ [%]	-48.6	+30.0	-65.3	+46.0	+46.9	-42.8	+68.6	-60.1	-15.3	-12.3	-26.7	-23.1

3.2 Isolated Offshore Island

This section assesses the limits to power extraction in the vicinity of an isolated offshore island of dimensions $L_i = B_i = 50h_o$, centred midway across the domain in the transverse direction, at a distance $s = 9.5\emptyset_i$ from the landmass. The computational mesh has 7,341 vertices and 14,682 elements (Figure 3*b*). Power is extracted south of the island over a rectangular area, of the same dimensions L_f x B_f as the farm in the strait of the island-landmass system, and extending south from the southern limit of the island. Both free-slip and no-slip scenarios are considered for the island, and the north and south domain limits are defined as free-slip boundaries.

Figure 12 compares the three-tidal-period-averaged $\overline{P}_{ko}$, $\overline{P}_s$, $\overline{P}_k$ and $\overline{P}_e$ profiles with k_f for the free-slip and no-slip scenarios. As for the island-landmass system, both free-slip and no-slip scenarios may represent lower and upper bounds to $\overline{P}_e$ in the vicinity of the island. There is no evident relationship between maximum $\overline{P}_e$ and $\overline{P}_s$ or $\overline{P}_{ko}$. For no-slip, the maximum $\overline{P}_e$ is 17 % lower than that reached in the island-landmass case, indicating that the presence of the landmass benefits power extraction from the coastal site. As in the island-landmass system, the rate of decrease of $\overline{P}_k$ at $k_f < 0.14$ is higher for the free-slip than for the no-slip condition. The ratios $\overline{Q}/\overline{Q}_o$ at maximum $\overline{P}_e$ are equal to 1.19 and 1.05 for the free-slip and no-slip scenarios respectively, indicating similar dynamic behaviour to the island-landmass system.

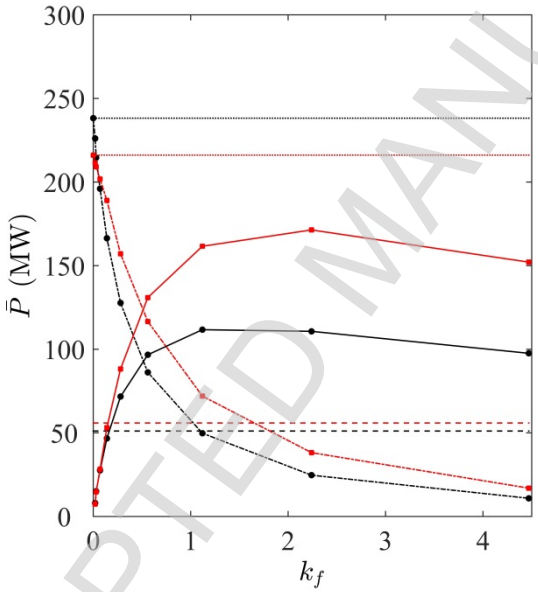

Figure 12. Power profiles as functions of k_f for a tidal farm located south of an isolated offshore island: free-slip (black); and no-slip (red) solid boundaries. Power extracted at farm located south of the island $\overline{P}_e$ (solid line); kinetic power measured across the tidal farm $\overline{P}_k$ (dash-dot line); kinetic power measured across the tidal farm in undisturbed conditions $\overline{P}_{ko}$ (dotted line); and natural power dissipated on the seabed south of the island $\overline{P}_s$ (dashed line).

3.3 Geometrically Long Island

This section analyses the sensitivity of the tidal resource at the strait to the length of the island. The length of the island is increased to $L_i = 800h_o$ while the width of the island and strait dimensions remain $B_i = s = 50h_o$. The computational mesh contains 19,335 vertices and 38,670 elements (Figure 3*c*). Power extraction is implemented in the strait over a rectangular area (of identical dimensions to that in the island-landmass system midway along the island in the

stream-wise direction). Figure 13 plots the three tidal period-averaged power parameters, $\overline{P}_{ko}$, $\overline{P}_s$, $\overline{P}_k$ and $\overline{P}_e$, obtained for the free-slip and no-slip scenarios when k_f is increased from 0 to 18. The larger seabed footprint covered by the island explains why $\overline{P}_s$ is three times greater than $\overline{P}_{ko}$. Maximum $\overline{P}_e$ is higher for free-slip than no-slip conditions. For the no-slip condition, maximum $\overline{P}_e$ is 95 % higher than for the island-landmass system, owing to the larger seabed footprint of the strait. The results indicate that $\overline{P}_s$ may provide a good approximation to maximum $\overline{P}_e$ in the strait. Both free-slip and no-slip scenarios present similar decay rates of $\overline{P}_k$ with power extraction.

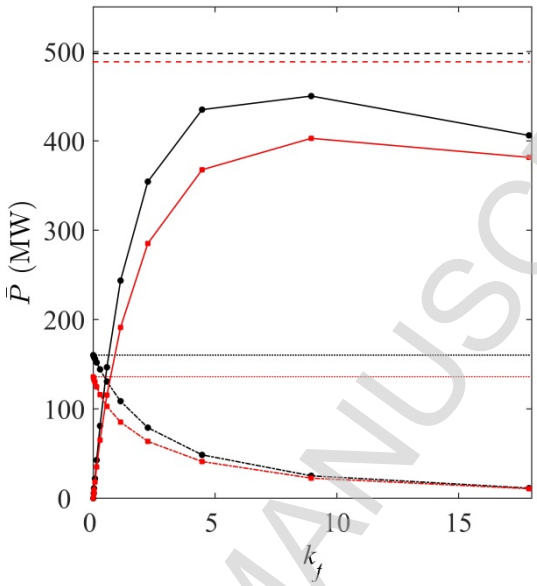

Figure 13. Power profiles as functions of k_f for a tidal farm located in a strait between a long elliptical island and a landmass: free-slip (black); and no-slip (red) solid boundaries. Power extracted at farm located south of the island $\overline{P}_e$ (solid line); kinetic power measured across the tidal farm $\overline{P}_k$ (dash-dot line); kinetic power measured across the tidal farm in undisturbed conditions $\overline{P}_{ko}$ (dotted line); and natural power dissipated on the seabed at the strait $\overline{P}_s$ (dashed line).

The ratio $\overline{Q}/\overline{Q}_o$ at maximum $\overline{P}_e$ is 1.03 for free-slip and 1.02 for no-slip. Figure 14 plots the head driving the flow in the strait for a case with no extraction and at maximum $\overline{P}_e$ (k_f =8.95) with free-slip. The observed increase in head amplitude is less than for the island-landmass system (Figure 8).

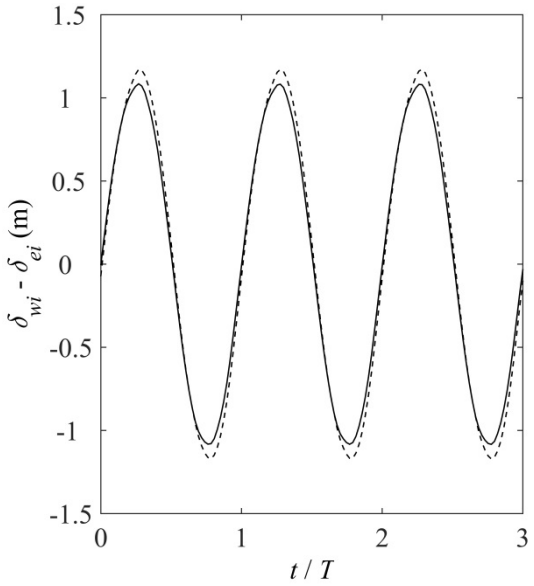

Figure 14. Tidal head difference between entrance and exit of the strait between a geometrically long island and mainland with free-slip condition at the island: no power extraction (solid line); very high extraction k_f = 8.95 (dashed line) in the strait.

Based on the tidal head difference and the maximum volumetric flow rate in undisturbed conditions with γ = 0.22 for the free-slip scenario, the GC2005 channel model predicts $\overline{P}_e$ = 411.4 MW, which is 8.6 % lower than the numerical prediction. For γ = 0.2 the $\overline{P}_e$ prediction using the GC2005 model is 16.9 % lower than the numerical value. Similar discrepancies between analytical and computed results are observed for the no-slip scenario. Although the GC2005 model appears to underestimate $\overline{P}_e$ relative to the numerical model, there is better agreement between the two approaches than for the island-landmass system. This indicates that the longer the island length, the more the strait dynamics resemble those in an idealised channel, in concurrence with a similar finding by Sutherland *et al*. [12] in a study of the Johnstone strait.

3.4 Geometrically wide island

This section assesses the effects of the width of the island on the resource in the strait. L_i and s are kept equal to $50h_o$ and the island width is increased to $B_i = 200h_o$. In order to keep the same domain blockage ratio, B is increased by a factor of 4. The computational mesh comprises 10,465 vertices and 20,930 elements (Figure 3*d*). A free-slip boundary condition is applied to both island and landmass boundaries, leading to large-scale vortical structures shedding from the island. Figure 15 plots the three-tidal-period-averaged power coefficients, $\overline{P}_{ko}$, $\overline{P}_s$, $\overline{P}_k$ and $\overline{P}_e$, as functions of k_f as its value is increased from 0 to 4.5. As in Section 3.1, maximum $\overline{P}_e$ is not well approximated by either $\overline{P}_{ko}$ or $\overline{P}_s$. Maximum $\overline{P}_e$ is found to be almost triple that of the no-slip scenario of the island-landmass system. The ratio $\overline{Q}/\overline{Q}_o$ at maximum $\overline{P}_e$ is equal to 1.08. $\overline{P}_k$ exhibits a higher rate of decrease than for the corresponding case in Section 3.1. Figure 16 plots the head driving the flow in the strait for no extraction and for an extraction level of k_f = 2.24. The fluctuation in the sinusoidal signal originates from eddy shedding in the lee of the island. The increase in head driving the flow with extraction level and the increase in path distance offshore of the island are the main reasons why maximum $\overline{P}_e$ is higher than for the island-landmass system.

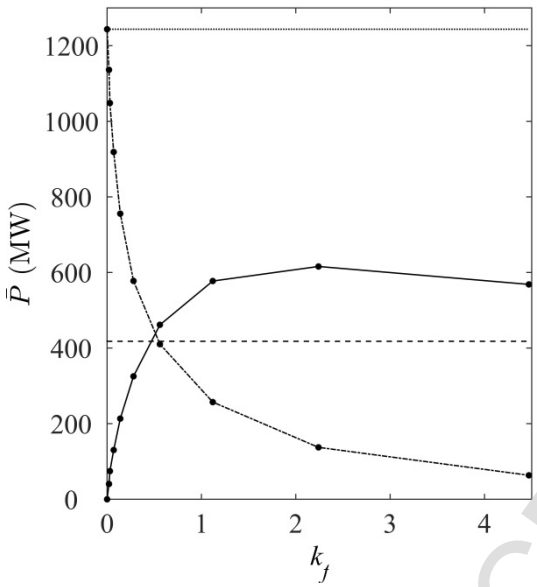

Figure 15. Power profiles as functions of k_f for a strait between an island with high width to length ratio and landmass. Extracted power for tidal farm located in the strait $\overline{P}_e$ (solid line); kinetic power for the strait with the tidal farm present $\overline{P}_k$ (dash-dot line); kinetic power for undisturbed conditions in the strait $\overline{P}_{ko}$ (dotted line); and natural power dissipated on the seabed at the strait $\overline{P}_s$ (dashed line).

Based on the flow conditions and head amplitude in the natural state, the GC2005 channel model predicts maximum power extracted of 169.5 and 161.8 MW for γ = 0.22 and 0.21 (derived from the phase difference between maximum head and flow in the strait) respectively. This value under-predicts the numerically computed results by 72.5 % and 73.7 % respectively. Perhaps a more suitable analytical model for geometrically wide islands is that recently derived by Mei [32] for barriers oriented orthogonal to landmass. Mei's analytical model can be used to compute the maximum head difference between a barrier and a landmass based on tidal frequency, maximum tidal flow velocity along the landmass without the barrier, gravitational acceleration, and the length of the barrier.

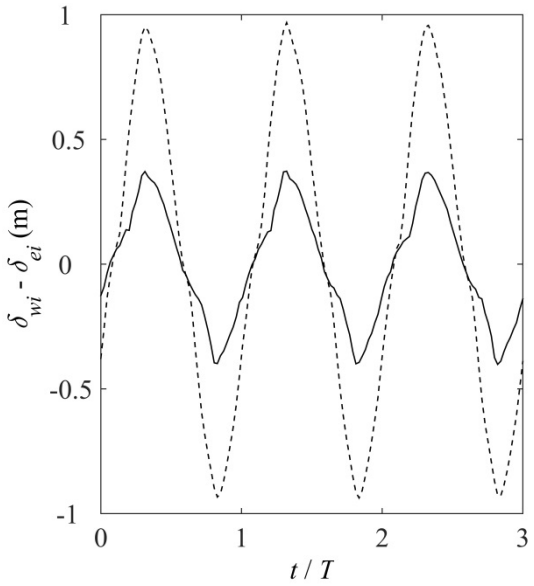

Figure 16. Flow driving head between the entrance and exit of the strait for the free-slip scenario of a geometrically wide island: no power extraction (solid line) and high extraction level k_f = 2.24 (dashed line) at the strait.

4 Conclusion

This paper has characterized numerically the tidal resource at idealised sites representing an island-landmass system. It is shown that the maximum power extracted in the strait between the island and landmass is generally not well approximated by either the power dissipated naturally at the seabed in the strait or by kinetic power in the absence of the turbines. Both parameters have been used in the past to assess the exploitable resource at tidal coastal sites. An exception is the case of a geometrically long island, where the maximum power extracted is reasonably well approximated by the power dissipated by seabed friction. No-slip and free-slip conditions applied to the island and landmass boundaries may provide lower and upper bounds to maximum power extraction in the strait.

The GC2005 model consistently predicts a lower value than the numerical prediction of maximum averaged power extracted in the strait. The longer the island, the better the agreement between the analytical and numerical predictions. Primary reasons for discrepancies between the numerical and analytical results are: the non-inclusion in the latter of changes to the head driving the flow due to power extraction in the strait; and flow diversion on the offshore side of the island.

The choice of parameters representing bed friction and eddy viscosity, which are commonly used to calibrate numerical models, is demonstrated to have a significant influence on the predicted value of power extracted in the strait. As would be expected, less extractable power is available in a strait with high bed friction. The results are much less sensitive to choice of eddy viscosity, with changes only becoming apparent at relatively high values (e.g. 100 m^2s^{-1}). Lower flow resistance in deeper water offshore of the island leads to reduced power extraction from the strait. This highlights the necessity for developers to be aware of the effect of far-field bathymetry.

The maximum power extracted from the strait reduces as the blockage decreases; this occurs because two additional bypass flow routes in the strait are available: one between the array and island; the other between the array and landmass. Bypass flow routes in the strait are relatively shallow, increasing flow resistance. A blockage ratio of 80 % yields similar maximum power extracted to that of 100 % blockage ratio. Reduction of strait blockage to 60 %, which included deep regions of the strait, leads to lower maximum power extracted than at the higher blockage values.

Power generation is similar in the strait and at the offshore side of the island for identical extraction levels. In this case, the total power generated is higher than for an equivalent extraction level applied solely to one side of the island. Inclusion of power extraction offshore of the island increases flow resistance along the bypass route which lowers bypass flow rates and velocity deficits; this is then converted into higher power outputs generated by the island-landmass system. This implies an opportunity for optimal power generation if the island-landmass system is considered as a two-flow path problem.

Analysis of power extraction off an isolated offshore island reveals that absence of a nearby landmass lowers the maximum power extracted from a coastal site. Maximum power extracted from the strait is found to increase with length and width of the island.

This study has provided a comprehensive characterization of the limits to power extraction in island-landmass systems, examined differences in estimates of maximum power extracted obtained using the undisturbed kinetic power and the power dissipated naturally at the seabed, and highlighted limitations in the applicability of an analytical channel model to island-landmass systems. This information should be of particular use to policy makers and tidal developers in preliminary assessment of coastal sites for tidal energy development.

Acknowledgements

This work was supported by General Electric Renewable Energy with funding from the ETI and the EPSRC through the Industrial Doctoral Centre for Offshore Renewable Energy (EP/J500847/1). The authors would like to thank the Applied Modelling and Computation Group at Imperial College of London for free access to the software Fluidity and their support. The authors would also like to thank Paul Vigars who has provided valuable insight.

References

[1] M. Tsoskounoglou, G. Ayerides, and E. Tritopoulou, “The end of cheap oil: Current status and prospects,” *Energy Policy*, vol. 36, no. 10, pp. 3797–3806, Oct. 2008.

[2] S. Shafiee and E. Topal, “When will fossil fuel reserves be diminished?,” *Energy Policy*, vol. 37, no. 1, pp. 181–189, Jan. 2009.

[3] Intergovernmental Panel on Climate Change, “Climate change 2001: Synthesis summary,” 2001.

[4] J. D. Boon, *Secrets of the tide. Tide and tidal current analysis and predictions, storm surges and sea level trends*. Chichester, UK: Horwood Publishing Limited, 2004, p. 212.

[5] C. Garrett and P. Cummins, "The power potential of tidal currents in channels," *Proc. R. Soc. A Math. Phys. Eng. Sci.*, vol. 461, no. 2060, pp. 2563–2572, Aug. 2005.

[6] J. Blanchfield, C. Garrett, P. Wild, and A. Rowe, "The extractable power from a channel linking a bay to the open ocean," *Proc. Inst. Mech. Eng. Part A J. Power Energy*, vol. 222, no. 3, pp. 289–297, May 2008.

[7] T. A. A. Adcock, S. Draper, and T. Nishino, "Tidal power generation - A review of hydrodynamic modelling," *Proc. Inst. Mech. Eng. Part A J. Power Energy*, vol. 229, no. 7, pp. 755–771, Feb. 2015.

[8] S. Draper, "Tidal stream energy extraction in coastal basins," Doctoral Thesis, University of Oxford, Oxford, United Kingdom, 2011.

[9] I. G. Bryden and S. J. Couch, "ME1—marine energy extraction: tidal resource analysis," *Renew. Energy*, vol. 31, no. 2, pp. 133–139, Feb. 2006.

[10] R. Vennell, "Estimating the power potential of tidal currents and the impact of power extraction on flow speeds," *Renew. Energy*, vol. 36, no. 12, pp. 3558–3565, Dec. 2011.

[11] S. Draper, T. A. A. Adcock, A. G. L. Borthwick, and G. T. Houlsby, "Estimate of the tidal stream power resource of the Pentland Firth," *Renew. Energy*, vol. 63, pp. 650–657, Mar. 2014.

[12] G. Sutherland, M. Foreman, and C. Garrett, "Tidal current energy assessment for Johnstone Strait, Vancouver Island," *Proc. Inst. Mech. Eng. Part A J. Power Energy*, vol. 221, no. 2, pp. 147–157, Jan. 2007.

[13] C. Garrett and P. Cummins, "Generating Power from Tidal Currents," *J. Waterw. Port, Coast. Ocean Eng.*, no. June, pp. 114–118, 2004.

[14] S. Draper, A. G. L. Borthwick, and G. T. Houlsby, "Energy potential of a tidal fence deployed near a coastal headland," *Philos. Trans. R. Soc. A Math. Phys. Eng. Sci.*, vol. 371, no. January, 2013.

[15] S. Serhadlıoğlu, T. A. A. Adcock, G. T. Houlsby, S. Draper, and A. G. L. Borthwick, "Tidal stream energy resource assessment of the Anglesey Skerries," *Int. J. Mar. Energy*, vol. 3–4, pp. e98–e111, Dec. 2013.

[16] S. Draper, T. A. A. Adcock, A. G. L. Borthwick, and G. T. Houlsby, "An electrical analogy for the Pentland Firth tidal stream power resource," *Proc. R. Soc. A Math. Phys. Eng. Sci.*, no. 470, p. 20, 2014.

[17] P. F. Cummins, "The extractable power from a split tidal channel: An equivalent circuit analysis," *Renew. Energy*, vol. 50, pp. 395–401, Feb. 2013.

[18] A. Pérez-Ortiz, A. G. L. Borthwick, H. Smith, P. Vigars, and Q. Xiao, "Tidal Resource in Strait between Island and Landmass," in *Proceedings of the 11th European Wave and Tidal Energy Conference*, 2015, pp. 1–10.

[19] A. Pérez-Ortiz, A. G. L. Borthwick, J. McNaughton, J. Pescatore, H. Smith, P. Vigars, and Q. Xiao, "Verification and validation of tidal resource assessment model for a strait between an island and a landmass," in *2nd Asian Wave and Tidal Energy Conference*, 2014, p. 5.

[20] C. J. Cotter, D. A. Ham, and C. C. Pain, "A mixed discontinuous/continuous finite element pair for shallow-water ocean modelling," *Ocean Model.*, vol. 26, no. 1–2, pp. 86–90, Jan. 2009.

[21] "Fluidity Manual," Applied Modelling and Computation Group, Department of Earth Science and Engineering, South Kensington Campus, Imperial College London, London, United Kingdom, Version 4.1.10, 2014.

[22] R. Martin-Short, J. Hill, S. C. Kramer, A. Avdis, P. A. Allison, and M. D. Piggott, "Tidal resource extraction in the Pentland Firth, UK: Potential impacts on flow regime and sediment transport in the Inner Sound of Stroma," *Renew. Energy*, vol. 76, pp. 596–607, Apr. 2015.

[23] J. Donea and A. Huerta, *Finite element methods for flow problems*. Chichester, UK: John Wiley & Sons, Ltd, 2003, p. 350.

[24] W. Rodi, *Turbulence Models and their Appliation in Hydraulics*, 2nd ed. International Association for Hydraulic Research, Delft, The Netherlands, 1984.

[25] T. A. A. Adcock, A. G. L. Borthwick, and G. T. Houlsby, "The open boundary problem in tidal basin modelling with energy extraction," in *Proceedings of the 9th European Wave and Tidal Energy Conference*, 2011, pp. 1–7.

[26] R. H. Karsten, J. M. McMillan, M. J. Lickley, and R. D. Haynes, "Assessment of tidal current energy in the Minas Passage, Bay of Fundy," *Proc. Inst. Mech. Eng. Part A J. Power Energy*, vol. 222, no. 5, pp. 493–507, Aug. 2008.

[27] R. Vennell, S. W. Funke, S. Draper, C. Stevens, and T. Divett, "Designing large arrays of tidal turbines: A synthesis and review," *Renew. Sustain. Energy Rev.*, vol. 41, pp. 454–472, Jan. 2015.

[28] C. Geuzaine and J. Remacle, "Gmsh: A 3D finite element mesh generator with built-in pre- and post- processing facilities," *Int. J. Numer. Methods Eng.*, vol. 0, pp. 1–24, 2009.

[29] I. G. Bryden and S. J. Couch, "How much energy can be extracted from moving water with a free surface: A question of importance in the field of tidal current energy?," *Renew. Energy*, vol. 32, no. 11, pp. 1961–1966, Sep. 2007.

[30] T. A. A. Adcock, S. Draper, G. T. Houlsby, A. G. L. Borthwick, and S. Serhadlıoğlu, "The available power from tidal stream turbines in the Pentland Firth," *Proc. R. Soc. A Math. Phys. Eng. Sci*, vol. 469, 2013.

[31] S. Baston and R. Harris, "Modelling the hydrodynamic characteristics of tidal flow in the Pentland Firth," in *9th European Wave and Tidal Energy Conference*, 2011, p. 7.

[32] V. Ramos and G. Iglesias, "Performance assessment of tidal stream turbines: a parametric approach," *Energy Convers. Manag.*, vol. 69, pp. 49–57, May 2013.

[33] T. Nishino and R. H. J. Willden, "The efficiency of an array of tidal turbines partially blocking a wide channel," *J. Fluid Mech.*, pp. 1–11, Aug. 2012.

[34] C. C. Mei, "Note on tidal diffraction by a coastal barrier," *Appl. Ocean Res.*, vol. 36, pp. 22–25, Jun. 2012.